CrossMark

A new type of linear magnetostrictive motor

Lucian Pîslaru-Dănescu[1] · Alexandu M. Morega[2,3] · Mihaela Morega[2] ·
Florentina Bunea[1] · Popa Marius[1] · Corina Alice Băbuţanu[1]

Abstract Magnetostrictive materials that may alter their shape significantly in response to external magnetic fields are used in unidirectional motion and force actuators and linear motors. In this study, we present a linear magnetostrictive motor (LMM) powered through a pulse width modulation (PWM) drive, whose core is a waveform controller of DRV101T type. Mathematical modeling and numerical simulations (in the finite element method) are used in the design phase to optimally size the LMM and to predict its behavior in stationary and dynamic working conditions, for a duty cycle (percentage of time when the driving coil is active) $k = 70\,\%$ and the frequency $f = 1$ kHz. The mechanical bias, provided by a spring system, is complemented with a bias coil, which is powered by a PWM stage too. This solution provides for enhanced and flexible control, while reducing the Joule losses to a minimum. LMM actuation is also provided through a second coil. The frequency of the voltage applied to the actuation coil is the same with the frequency of voltage applied to the bias coil. The concept of the LMM drive and its construction are validated through interferometry, vibration and thermal imager measurements.

✉ Lucian Pîslaru-Dănescu
  lucian.pislaru@icpe-ca.ro

1 Department for Efficiency in Conversion and Usage of Energy, National Institute for Research and Development in Electrical Engineering ICPE-CA, Bucharest 030138, Romania

2 Faculty of Electrical Engineering, University Politehnica of Bucharest, 060042 Bucharest, Romania

3 "Gh. Mihoc–C. Iacob" Institute of Statistical Mathematics and Applied Mathematics, Romanian Academy, 050711 Bucharest, Romania

1 Introduction

Recently, there is a growing interest in developing unidirectional motion and force actuators and linear motors based on the magnetostrictive materials such as Terfenol-D [1], which may alter their shape and size significantly in response to external magnetic fields, phenomenon which is known as magnetostriction [2,3].

Magnetostriction is responsible for the deformations in the crystalline structure of the magnetostrictive material, which results in changes in its elastic modulus. In general, when magnetization varies the elasticity modulus also varies and changes in the resonance frequencies of the magnetostrictive material also occur. Depending on the material, the relative variation of the elastic modulus is between 15 % (for nickel) and 190 % (for Terfenol-D), in an external magnetic field of strength $H = 240$ kA/m [3–5].

Of all commercially available magnetostrictive materials that exhibit large strains in magnetic fields, called giant magnetostrictive materials (GMM) [4], Terfenol-D has the largest known striction at ambient temperatures, namely 2000 ppm. The deformation of Terfenol-D depends on the direction of the external magnetic field: elongation in the field direction and contraction in the directions orthogonal on the magnetic field. This behaviour may be utilized in the construction of a short stroke actuator for applications that necessitate large forces at both high and low actuating frequencies, of interest in many applications, such as surgical instruments, ultrasonic transducers, injectors, etc. [6–9].

In this study, we present a linear magnetostrictive motor (LMM), which may be used as an actuator. The design concept of composite smart structure (CSS) [10,11] is used here for manufacturing parts of the LMM. Along this line, the morphing structure is a new, recently developed CSS concept and the sizing of the Terfenol-D part fits the definition. An illustrative example is provided in [12].

The LMM is built for optimal performance and packaging. To this end, we use mathematical modelling and numerical simulations, e.g., [13], which besides the ability of revealing meaningful insights in the physics of LMM are meaningful tools in the design sizing phase. Numerical simulations are based on fully coupled magneto-elastic finite element models (FEM) that implement the bidirectional coupling between the magnetic field and structural problems.

The LMM is powered by a PWM drive and both types of analyses, stationary (needed for sizing the LMM) and dynamic (needed to model the real working conditions), are used to validate the design. This approach proves to be realistic, capable of reproducing stationary and dynamic working conditions similar to those for which the LMM is intended. The main design phases, from concept to prototype and tests, are detailed in the sections that follow.

It is worth noting that our LMM presents several novel elements. For instance, the powering system that provides the bias magnetic field, which replaces the common hollow cylindrical permanent magnet [14], is made of a field coil and a permanent magnet.

Also, unlike conventional systems, the field coil (FC) of the LMM is powered with pulse width modulated (PWM) voltage of the same frequency and duty cycle as the activation coil (AC), rather than with a direct current. This way, Joule dissipation is minimized. The AC is powered with a PWM voltage with a duty cycle (percentage of time when the driving coil is active) $k = 10$–80 %. This approach provides for the stable operation of the LMM, for a frequency range $f = 0.5\,\text{Hz} \div 16\,\text{KHz}$.

In what follows, we present first the LMM concept and prototype; next, the mathematical model and the numerical simulation technique that were used in the earlier stages of design with the aim of optimally size the electromechanical part of the LMM. The numerical simulation results obtained for dynamic working conditions (powering scheme) were good predictive estimators of the LMM behaviour for a wide range of PWM duty cycles and frequencies. A discussion of the drive concept of the LMM follows. The experimental results presented thereafter substantiate the technical value of the prototype and its compliance with the assumed working conditions.
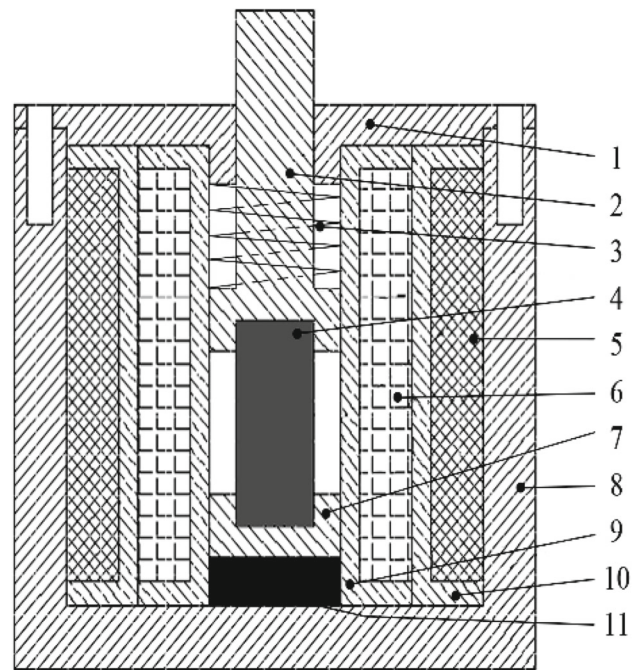

Fig. 1 The linear magnetostrictive motor: *1* casing cover, *2* workhead pin, *3* spring for pretension, *4* Terfenol-D, *5* bias coil, *6* activation coil, *7* lower pivot, *8* casing, *9* support for the activation coil, *10* support for the bias coil, *11* permanent magnet for bias

2 The linear magnetostrictive motor

The LMM is made of three main subassemblies, Figs. 1 and 2, as follows.

(A) *The active central subassembly* consists of an active magnetostrictive material core (MSC) (4) made of Terfenol-D ($\text{Tb}_{0.3}\,\text{Dy}_{0.7}\,\text{Fe}_{1.9-1.95}$). Its deformation capacity is in the range $800 \div 1200$ ppm. The MSC acts upon an upper pivot ("workhead pin") (2). An N35SH permanent magnet of cylindrical shape (11) contributes to the bias magnetic field. Its demagnetization temperature is 150°C minimum. Subassembly (A) contains also a pretension spring (with the elastic constant $K = 5153$ N/m) for mechanical bias (3) and a lower pivot (7), to support the MSC.

(B) *The coil subassembly* consists of a 1-mm thick-walled polytetrafluoroethylene (Teflon PTFE) case for the activation coil (9), the activation coil made of CuEm (6), with $N_A = 140$ turns and $\Phi = 0.6$ mm in diameter (measured without the insulating enamel), the 1-mm thick-walled Teflon PTFE case for the magnetic bias coil (10), the bias coil made of CuEm (5), with $N_B = 145$ turns and $\Phi = 0.6$ mm in diameter (measured without enamel). The two coils are impregnated with 525Ez insulating varnish.
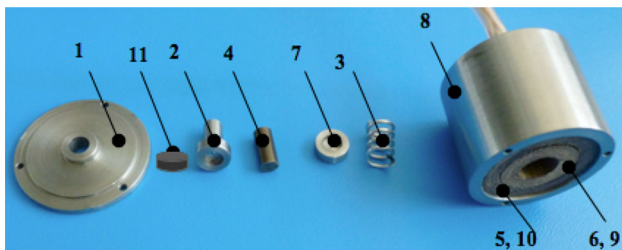
Fig. 2 The LMM prototype

The electrical properties of the two coils were measured with Agilent's E4980A precision RLC-bridge. At $f = 5\,\text{kHz}$, the activation coil (6) shows off, for the parallel equivalent scheme: the inductivity $L_P = 245\,\mu\text{H}$, the resistance $R_P = 23.8\,\Omega$ and the quality factor $Q_P = 3.1$, where $Q_P = \sqrt{\frac{C}{L_P}} R_P$, C [F] is the electrical capacity between the turns and for the equivalent series scheme: $L_S = 222\,\mu\text{H}$, $R_S = 2.26\,\Omega$ and $Q_S = 3.1$, where $Q_S = \sqrt{\frac{L_S}{C} \frac{1}{R_S}}$. The continuous current (DC) resistance is $DRC = 452\,\text{m}\Omega$.

At $f = 5\,\text{kHz}$, the magnetic bias coil (5) shows off for the parallel equivalent scheme: $L_P = 457\,\mu\text{H}$, $R_P = 42.62\,\Omega$ and $Q = 3$ and for the equivalent series scheme, $L_S = 410\,\mu\text{H}$, $R_S = 4.37\,\Omega$ and $Q = 3$. The DC resistance is $DRC = 700\,\text{m}\Omega$.

(C) *The casing subassembly* consists of a cylindrical shell (8) and an intermediate cover (1), both of which are made of low magnetic remanence AISI 420 stainless steel, with relative magnetic permeability $\mu_r = 950$ [15].

The LMM prototype was manufactured at the National Institute for Research and Development in Electrical Engineering, ICPE-CA, Romania.

3 Mathematical modelling and numerical simulation of the linear magnetostrictive motor

3.1 The mathematical model

The mathematical model of the magnetic field and structural interactions that occur in the LMM rely on the apparent axial symmetry of the device, which may be used to reduce the computational domain (Fig. 3,a) and the pending numerical effort and computer time. Although simplified to discard finer details that are irrelevant at this stage, the model bears the main magnetic and mechanical features of the real life device. This 2D axial-symmetric approach provides for accurate results, relevant and useful in the design stage.

Figure 3b shows the unstructured finite element (FEM) mesh made of $\sim 10,000$ second-order Lagrange elements that was used to solve for the magnetic field problem and
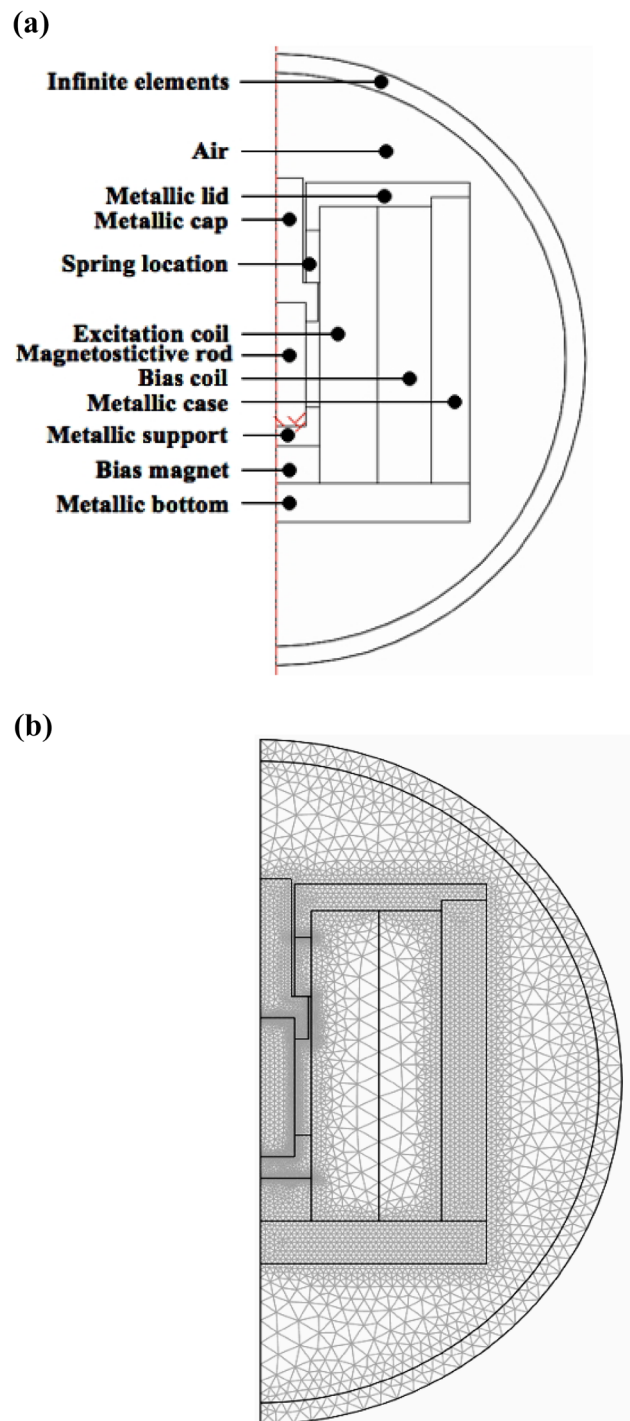
(a)

(b)

Fig. 3 The 2D model for the linear magnetostrictive motor (LMM) with a master magnetostrictive core (MSC). **a** The computational domain. **b** The unstructured finite element mesh used in the numerical simulations

quadratic Lagrange elements were used for the structural problem.

The magnetic bias is provided by a cylindrical permanent magnet–bias coil arrangement. The MSC deforms when the

driving coil is powered. The action of a pre-stressing spring is accounted for. The following main assumptions are used:

- The MSC is in a pre-stressed state that would yield maximum magnetostriction.
- The magnetization curve of the magnetostrictive material is non-linear.
- The saturation effect in the magnetic circuit at high magnetic fields is accounted for.
- The coils are modelled as equivalent (homogenized) electro-conductive domains, where the individual wires are not discernible.
- Inductive and skin effects are discarded.

The magnetic field problem is described through the azimuthal induction currents model [12,13]:

within the magnetostrictive material core

$$\sigma \frac{\partial \mathbf{A}}{\partial t} + \nabla \times \mathbf{H} = 0, \quad \mathbf{A} = A_\varphi \mathbf{e}_\varphi, \tag{1}$$

within all other parts

$$\sigma \frac{\partial \mathbf{A}}{\partial t} + \nabla \times \left[\mu_0^{-1} \mu_r^{-1} \left(\nabla \times \mathbf{A} - \mathbf{B}_{rem} \right) \right] = \mathbf{J}_\varphi^e, \quad \mathbf{A} = A_\varphi \mathbf{e}_\varphi, \tag{2}$$

where $\mathbf{A}$ [T · m] is the magnetic vector potential, $\mathbf{H}$ [A/m] is the magnetic field strength, $\mathbf{J}_\varphi^e$ [A/m^2] is the azimuthal electrical current density (in the coils only), $\mathbf{B}_{rem}$ [T] is the remanent magnetic flux density of the permanent magnet and μ_r is its relative permeability. The magnetic core is made of soft iron without losses (Fig. 4a) and the MSC of Terfenol-D (Fig. 4b).

A layer of infinite elements (Fig. 3a) bounds the computational domain for the magnetic field problem, of "open space" type, within a finite distance. The boundary conditions are: symmetry for the Oz axis and magnetic insulation ($\mathbf{n} \times \mathbf{A} = 0$, where $\mathbf{n}$ is the outer normal) on the rest of the boundary.

The structural stress–strain axial model concerns the MSC, the upper and lower magnets and the metallic workhead pin on top. Magnetostriction does not produce stress in the MSC unless this one is constrained. The axial deformation of the MSC, which may exhibit significant strain, is described by a generalized Hooke's law [12,13,16]

$$[\sigma] = [C] \{[\varepsilon] - [\varepsilon_i]\} + [\sigma_i], \tag{3}$$

where $[C]$ is the stiffness matrix, $[\varepsilon]$ is the strain, $[\varepsilon_i]$ is the initial strain, $[\sigma]$ is the stress and $[\sigma_i]$ is the pre-stress. The MSC is pre-stressed to provide for a maximum magnetostrictive effect.
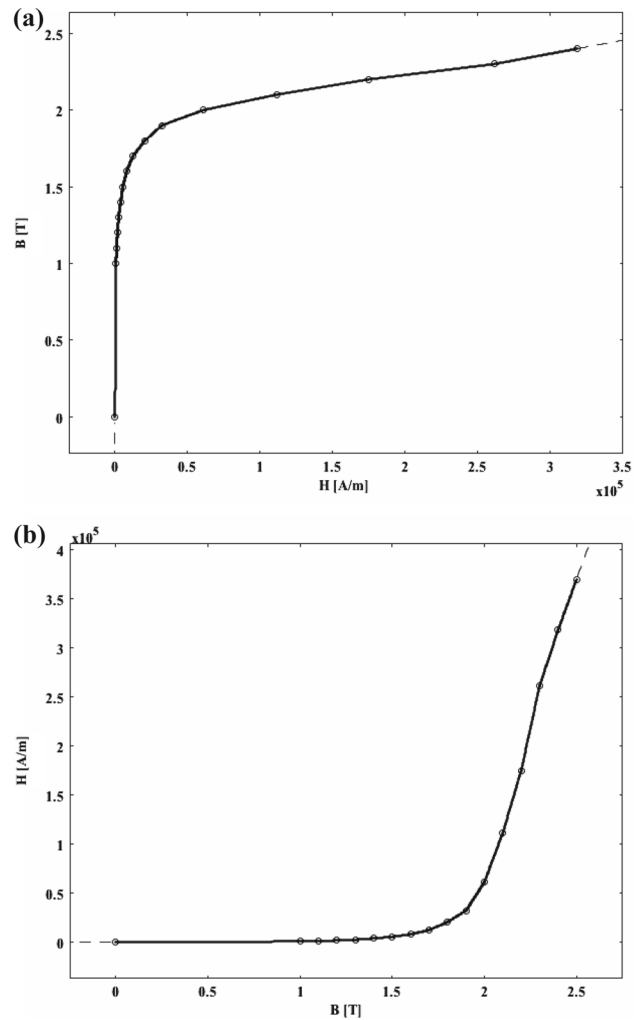
Fig. 4 Magnetic properties of active magnetic materials. **a** The soft iron core [15]. **b** Terfenol-D [1]

The non-linear relation between the magnetic field and the mechanical stress introduces the magnetostriction coefficient in Or and Oz directions, $\lambda_{r,z}$, which depends on the magnetostriction constant, λ_S and the direction of magnetization (here, Oz).

$$\lambda_{r,z} = \frac{3}{2} \lambda_S \left(\alpha_{r,z}^2 - \frac{1}{3} \right) = \frac{3}{2} \lambda_S \left[\left(\frac{M_{r,z}}{M_S} \right)^2 - \frac{1}{3} \right], \tag{4}$$

Magnetostriction, λ_i, along the direction i depends on the magnetostriction constant, λ_s and the magnetization direction, $\cos(\alpha_i)$. The directional cosine is the ratio of magnetization along the required direction, M_i, and the saturation magnetization of the material, M_S. The random orientation of the magnetic moments in the MSC in the absence of any magnetic field is accounted for by the 1/3 term. Assuming that the material is sufficiently pre-stressed such that all magnetic moments are perpendicular to the direction of magnetization

at the beginning of the magnetization process, we may ignore the 1/3 term, *i.e.*, the MSC in a pre-stressed state would yield maximum magnetostriction [3].

The boundary conditions that close the structural model are symmetry, for the sides on the symmetry axis, "fixed" for the bottom, load for the shoulder that supports the spring and "free" (unconstrained) for the rest. The mathematical model is then FEM [17] solved.

3.2 Numerical simulation results and discussion

3.2.1 Stationary working conditions

The stationary analysis, conducted for no mechanical load, is aimed at discovering the magnetic field critical regions, namely those parts with high magnetic flux density, which are prone to saturation, the mechanical behaviour of the device

Fig. 5 Stationary and dynamic displacement in the LMM for $k = 70\%$ and $f = 1$ kHz. Stationary working conditions. **a** The magnetic flux density (streamlines) and the mechanical displacement. **b** Detailed view. The maximum mechanical displacement is $\sim 2.8\,\mu$m
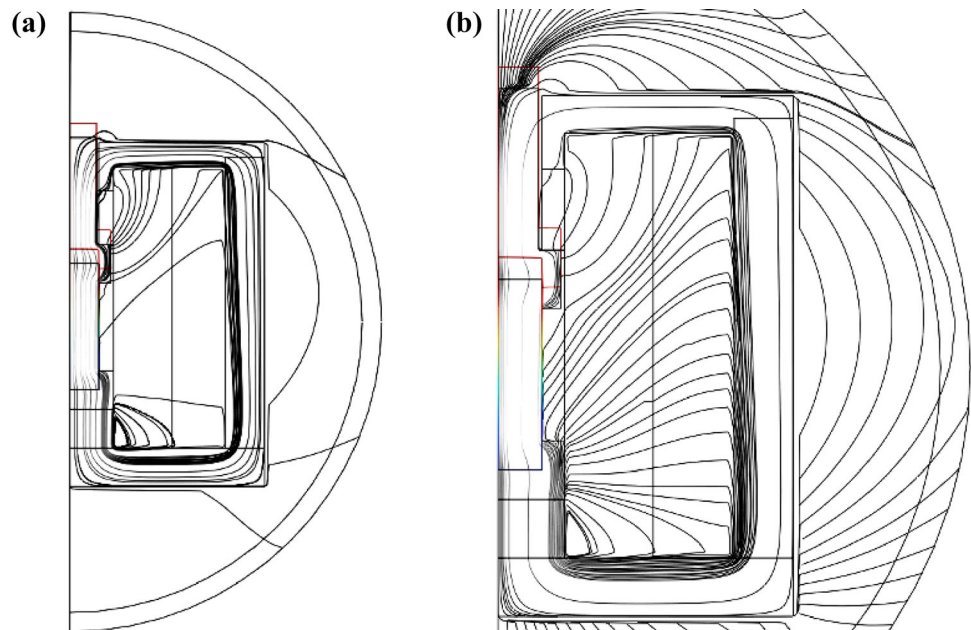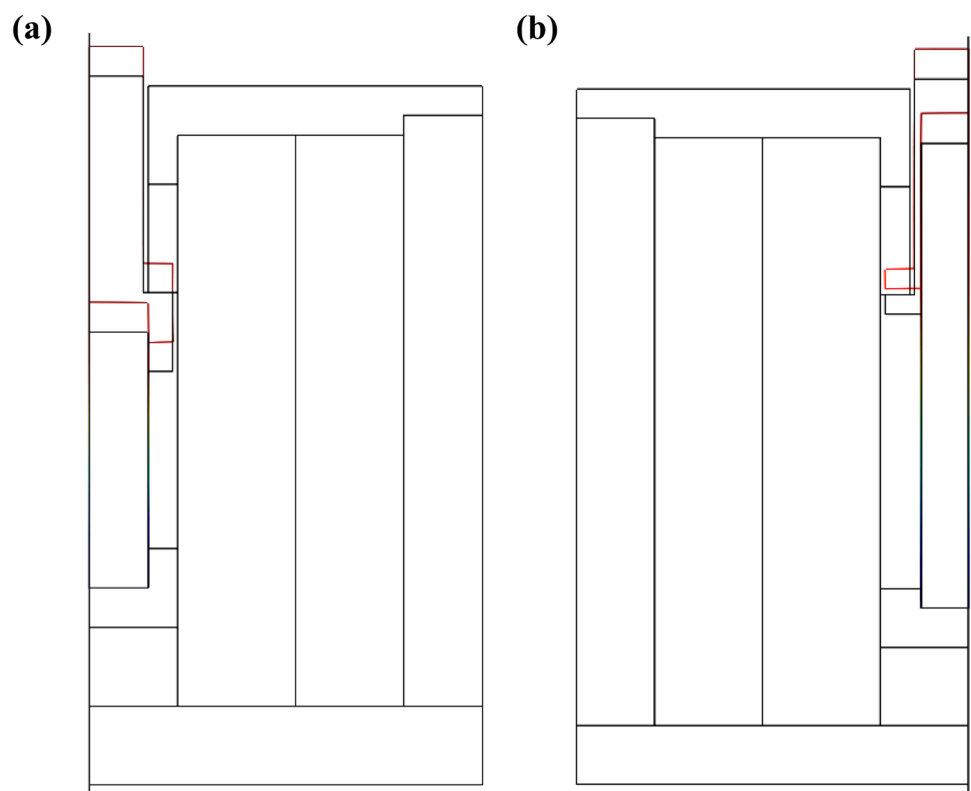

Fig. 6 Two designs for the MSC of the same LMM. The MSC volume is kept constant. Deformations, marked in red, are amplified for better viewing. **a** For the master MSC shape (AR = 4), the maximum displacement is $\sim 2.8\,\mu$m. **b** For the optimized MSC (AR = 8.1), the maximum displacement is $\sim 4.7\,\mu$m

(the displacement of the mobile piece). The outcome is a first-stage optimization of the LMM.

Figure 5 shows the magnetic flux density ($B_{max} = 2.05$ T) and the displacement ($\sim 2.8\,\mu$m) for stationary working conditions.

An important optimization parameter is the geometric aspect ratio (height/width), AR, of the MSC. This quantity is here a degree of freedom. The initial AR (Figs. 5, 6,a) is the "reference" or "master" shape of the MSC, and the volume of the MSC, assumed constant, is a design parameter: the amount of magnetostrictive material that the designer decides to use. Figure 6 shows the deformations for two MSC designs, the reference case and the optimized core.

The AR of the MSC is parameterized, while the volume of the MSC, the other parts of the LMM and the electrical currents are kept unchanged. The slender the MSC, the larger is

its deformation. However, magnetic saturation occurs for too slender cores. It is expected then that an optimal AR exists for which the deformation is large enough, while the saturation level is acceptable for the LMM to work as a liner actuator.

The efforts devoted to explore this optimization venue and the results obtained for no mechanical load and for several load conditions, for a range of MSC volumes, are presented in [12].

The complementary heat transfer analysis of the LMM, an important design problem, makes the object of future research. The results will be used as initial conditions in the optimization project of the LMM under dynamic working conditions.

3.2.2 Dynamic working conditions

We present here the numerical simulation results for $k = 70$ %, at $f = 1$ kHz. The diagrams of the PWM bias and
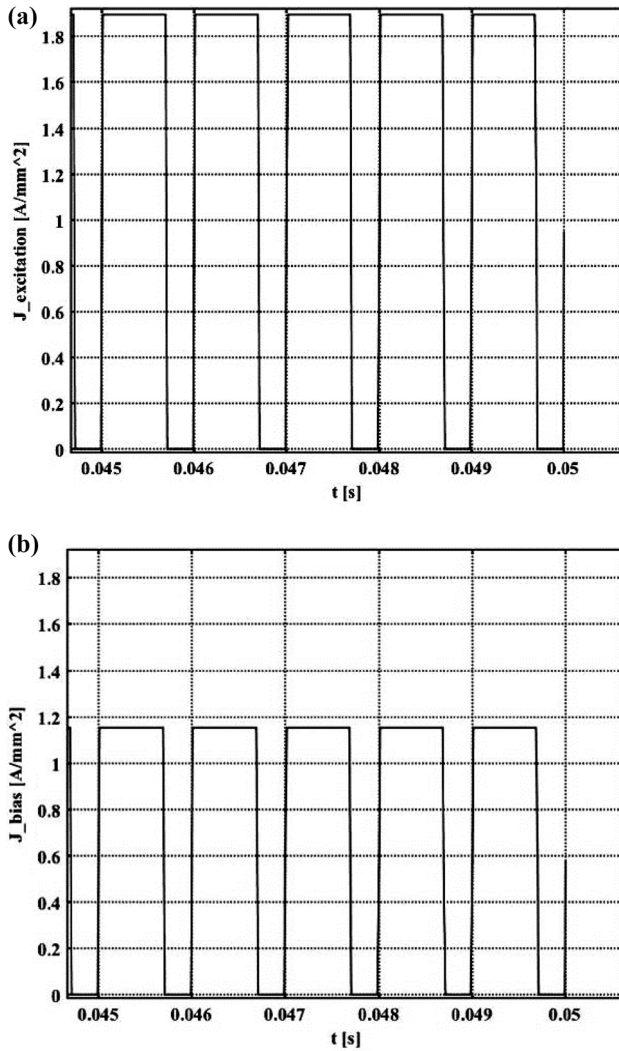

Fig. 7 The electrical current densities in the LMM coils. The duty factor $k = 70\%$ and the PWM underlying frequency is $f = 1$ kHz— equivalent electrical current densities. **a** The field current within the bias coil (Fig. 1). **b** The driving current (the inner coil, Fig. 1)
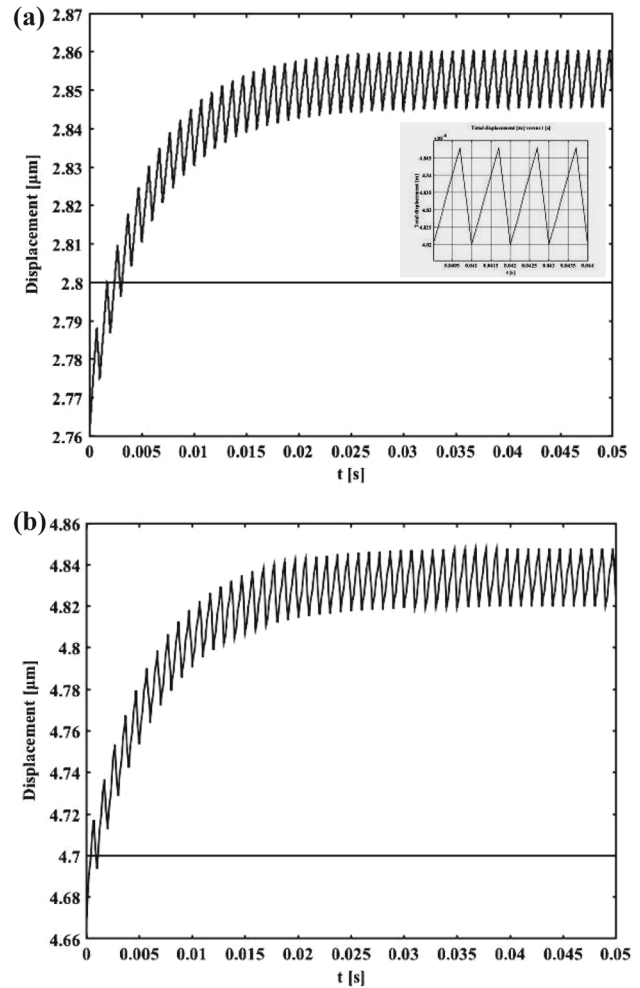

Fig. 8 The effect of the MSC aspect ratio on the mechanical displacement for stationary and dynamic working conditions. Stationary results are marked through straight lines. **a** The master MSC. **b** The optimized MSC

actuation currents (with the same k) are shown in Fig. 7. In the boundary and initial value problem (1)–(4) the power sources are treated as current sources and the electrical current density (the source term in problem (2)) is modelled using delayed Heaviside functions (Fig. 7) that may synthesize step functions with controllable numerical accuracy.

Figure 8 shows the displacement of the workhead pin [(2) in Fig. 1] for dynamic (quasi-steady) working conditions. The output signal (the pin displacement) may be controlled, for instance, by adjusting the field currents (excitation and bias). This effect will be investigated in the proposed research.

The details in Fig. 8a indicates that, for the assumed working conditions, the dynamics of displacement for this LMM is basically quasi-linear.

4 The concept of the new drive for the LMM

The construction, whose electronic design is illustrated in Figs. 9 and 10, is centered on the use of the PWM waveform controller DRV101T, made by Burr-Brown & Texas Instruments Company [18]. This drive has certain specific features, highlighted next.

First, as seen in Figs. 9 and 10, we use a different method of powering through using direct current in the power output stage, respectively, in the controller. Thus, the power output stage is powered by an external DC of Agilent's U 8031 A type, which can provide a stabilized voltage of $+24\,V_{DC}$, for

$I_{\max} = 4$ A. The PWM waveform controller and the ancillary electronic circuits are powered through an internal stabilized voltage source of 24 V_{DC} for $I_{\max} = 1$ A. This particular kind of feeding DC current allows us attachment of any type of linear actuator, such as the LMM. The only limiting factor is the drain-source voltages of the isolate gate bipolar transistors (IGBTs), T_4, T_5, T_9, T_{10}, of type IRG4PH40KDPbF (Fig. 10) and the drain current of the transistors, I_D. In this case, the maximum current through the activation coil of the LMM may be $I_{\mathrm{Amax}} = 4$ A, if the maximum activation voltage, PWM, is about $U_{\max} = 100\,V_{PP}$ (peak to peak).

If at the input pin of the PWM DRV101T waveform controller (pin 1 in Fig. 10), a rectangular-shaped TTL signal, $U_{\mathrm{d}} = +5V_{PP}$ and $f = 1$ Hz $\div$ 16 kHz is applied (e.g., through using an external signal generator of type FLUKE 281), the active magnetostrictive material core (MSC) of the LMM oscillates, causing the MSC to perform synchronously a linear, alternating, periodic motion. The duty cycle of the control voltages applied to the complementary transistors (T_1, T_2 respectively T_6, T_7) of BD 139 and BD 140 type [19,20] respectively retrieved to the grid of the IGBT transistor (T_3, T_8) of type T3G7N60C3 (Fig. 10), can vary within $k = 1 \div 99$ %.

The waveform of the voltage applied to the activation coil of the LMM, with $f = 10$ Hz and $k = 10$ %, is illustrated in Fig. 9. Similarly, the waveform of the voltage applied to the activation coil of the LMM, for $f = 10$ Hz and $k = 40$ %, is illustrated in Fig. 10. The waveforms in Figs. 11 and 12

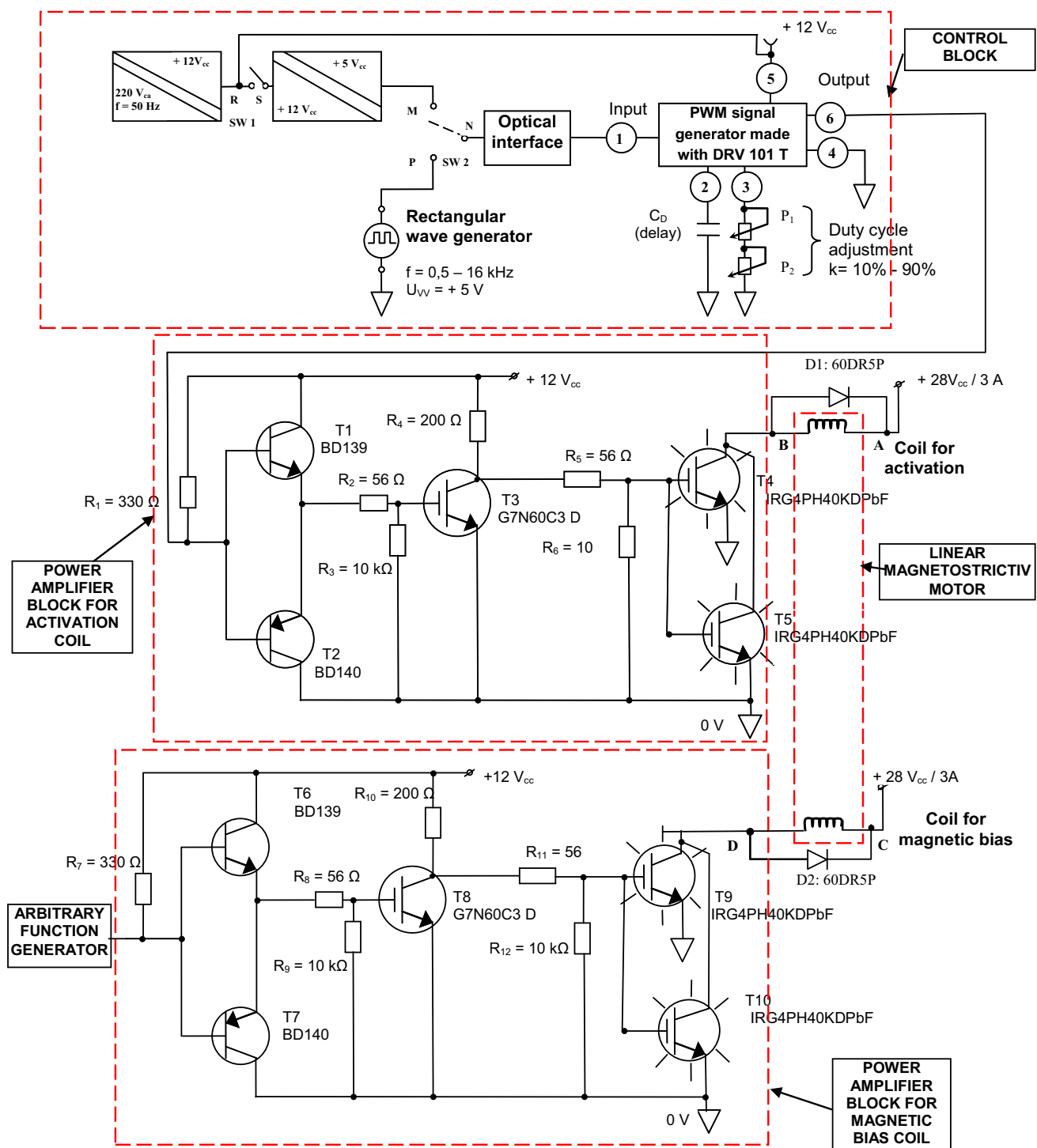**Fig. 9** The block diagram of the drive electronic module
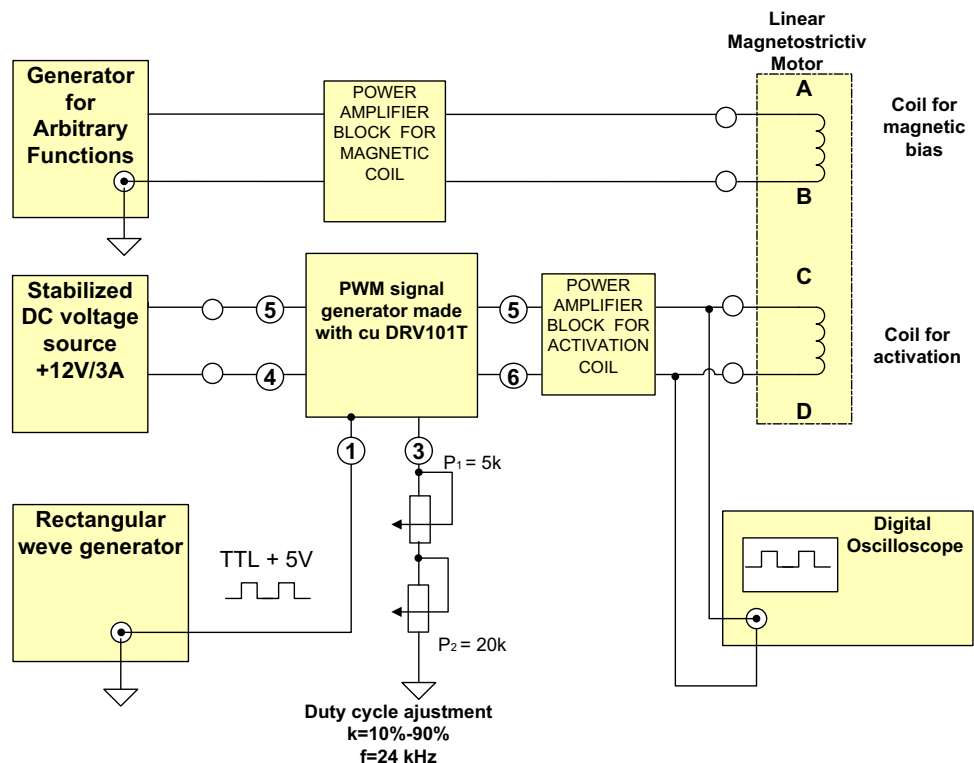
Fig. 10 The electronic circuit designed for the activation drive of the LMM

were obtained using a digital FLUKE 196C oscilloscope and FLUKE VIEW acquisition software.

Between the isolate gate bipolar transistor (IGBT) power grid (model IRG4PH40KDPbF), which is directed with voltage impulses, and the DRV101T controller output (pin 6, Fig. 10) there is an IGBT electronic buffer made of the complementary transistors BD 139 and BD 140 [19,20], respectively, the IGBT transistor of type T3G7N60C with its ancillary passive components.

During the process of "linear actuation" the signal "1" (in TTL logic) is sent along the controller input (pin 1, Fig. 10). Thus, the LMM can operate in a "linear mode" and the duty
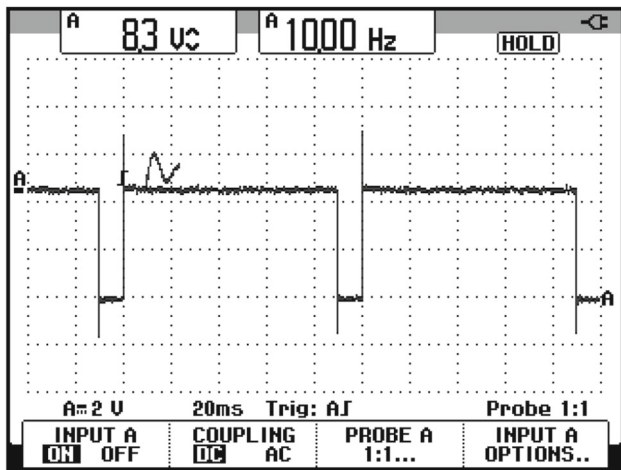
Fig. 11 Waveform of applied voltage to the activation coil of the LMM at $f = 10$ Hz for $k = 10$ %
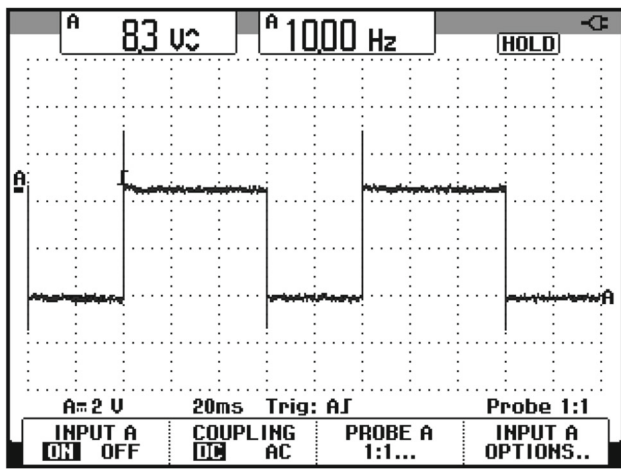

Fig. 12 Waveform of applied voltage to the activation coil of the LMM at $f = 10$ Hz for $k = 40$ %

cycle of the control voltage, applied to the complementary transistors BD 139 and BD 140, respectively, to the IGBT transistor grid [13] of type T3G7N60C3 (Fig. 10) is allowed to vary [14] within the range $k = 10 \div 90$ % for a constant frequency, $f = 24$ kHz.

The signal "1" (in TTL logic) is applied first at the microcontroller input via an optical interface, designed with a TTL optocoupler of type HCPL 2639 (Fig. 10).

5 Experiments on the LMM

Interferometry, vibration and thermal imager measurements were performed to characterize the LMM functioning. The mechanical oscillations of the MSC were measured for two different frequencies, 100 Hz and 5 kHz.

For $f = 100$ Hz (Fig. 13), the mechanical oscillation amplitude is $A = 0.3 \, \mu$m and for $f = 5$ kHz (Fig. 14) $A = 0.04 \, \mu$m. The measurements are performed with a system that includes an interferometer Agilent 5529B with the linear measurement kit 55280A (Figs. 15, 16).

The experiments presented here correspond to the case when the activation coil (Fig. 1) is energized, through its power amplifier block (Fig. 10), with U_1 voltage of PWM_1 form. The magnetic bias coil (Fig. 1) is energized, through its power amplifier block (Fig. 10), with U_2 voltage of PWM_2 form. The frequency and the peak-to-peak value of the voltages U_1 and U_2 are the same, namely $f = 0.5$ Hz $\div 12$ kHz and 12 V_{PP}, respectively. The duty cycle of U_1 is $k = 80$ % and the duty cycle of U_2 is $k_B = 50$ %. As a direct consequence, the Joule–Lenz losses are drastically reduced. Recall that the magnetic bias is produced through the cumulative effect of the constant magnetic field produced by the permanent magnet (position 11 in Fig. 1) and of another pulsating
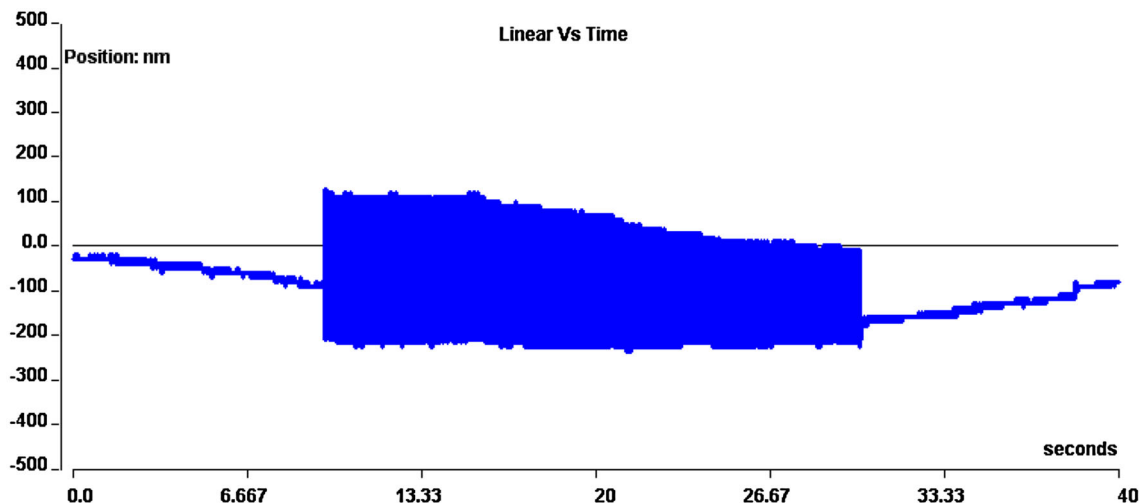

Fig. 13 Mechanical oscillation amplitude diagram for the MSC at $f = 100$ Hz, $A = 12 \, V_{PP}$ and $k = 80$ %
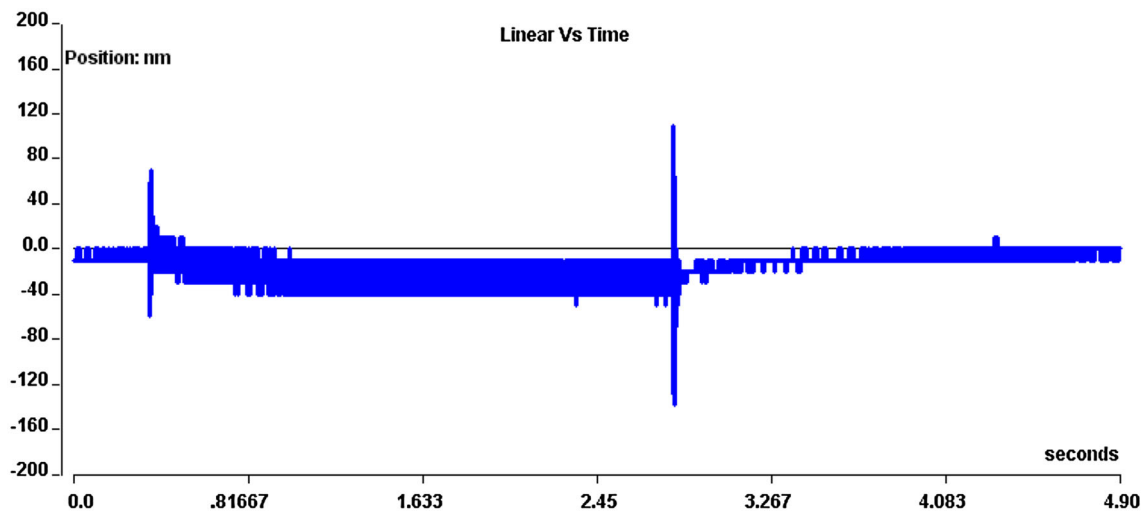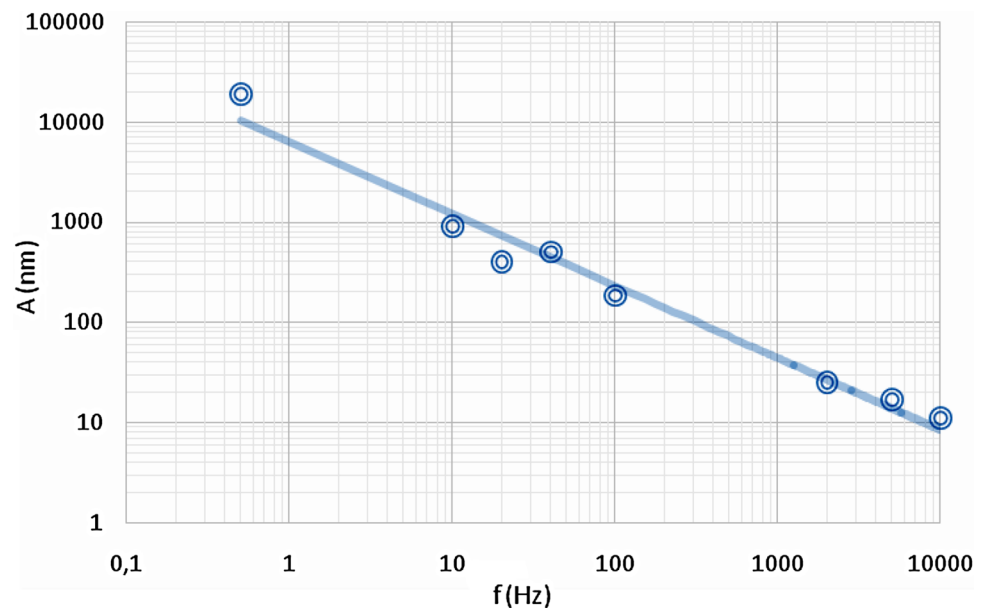
Fig. 14 Mechanical oscillation amplitude diagram for the MSC at $f = 5$ kHz, $A = 12$ V$_{PP}$ and $k = 80$ %

Fig. 15 Amplitude variation of the mechanical oscillation of the MSC at $A = 12 V_{PP}$ and $k = 80$ %

magnetic field, produced by the electrical current in the magnetic bias coil.

The results obtained from the amplitude diagrams for eight different frequencies are synthesized in Fig. 15. Through plotting these results using a logarithmic scale for frequency, a linear characteristic is obtained.

This result suggests that the amplitude is an exponential function of the PWM underlying frequency—a valuable finding useful in the design of the LMM control.

Figure 17 shows the fast Fourier transform (FFT) of the MSC acceleration, for the fundamental frequency $f = 2500$ Hz. The two harmonics which accompany the fundamental have the frequencies $f_{A1} = 1.6$ kHz and $f_{A2} = 2$ kHz. The amplitude of those harmonics is 0.018 ms^{-2},
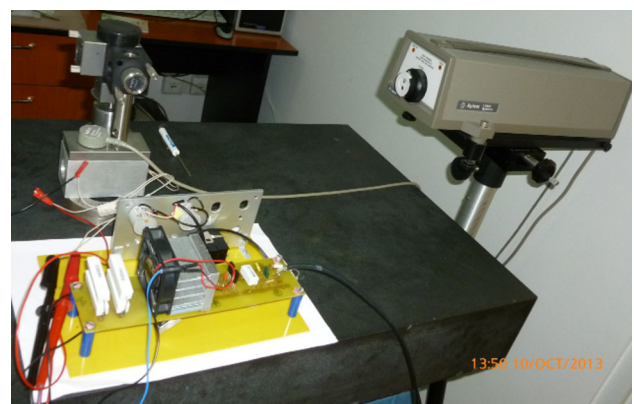

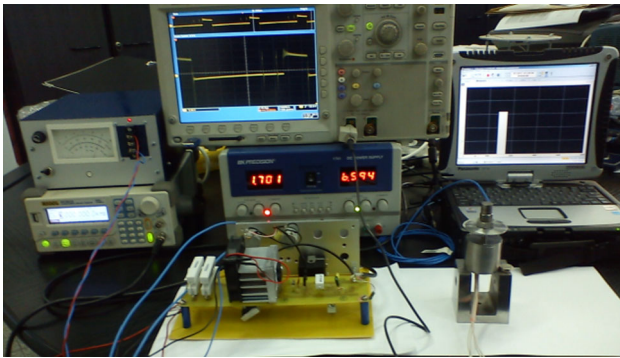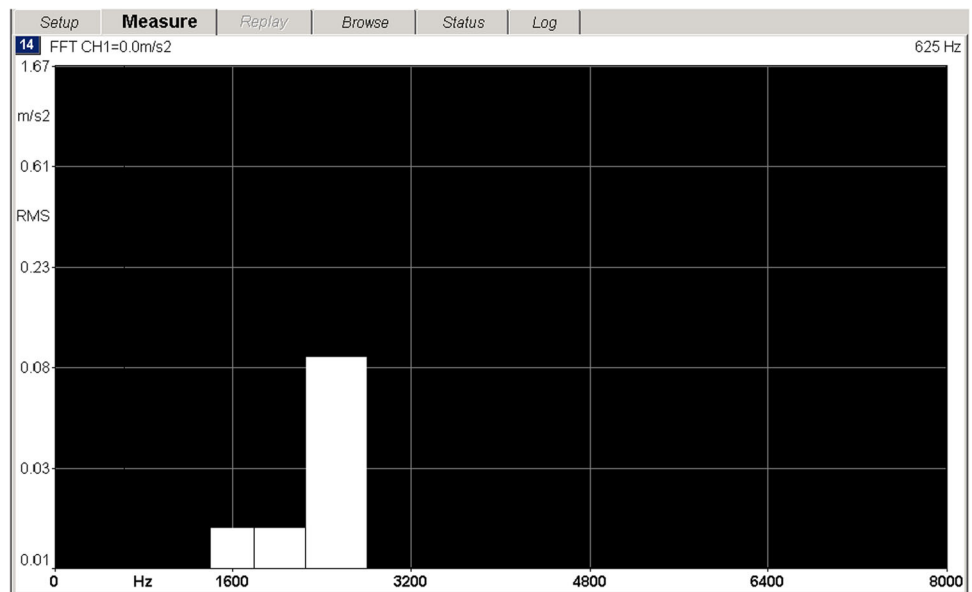**Fig. 16** The experimental layout used in interferometry measurements

Fig. 18 The experimental layout used for the mechanical vibration measurements. The LMM is marked for singling out

while the amplitude of the fundamental is much smaller ($0.082\,\text{ms}^{-2}$).

The system used to measure mechanical vibrations is made by Panasonic and uses an accelerometer of PCB353B03 type and Soundbook software (Fig. 18).

Fig. 19 presents the temperature field on the LMM after 1 h of operation. The maximum temperature recorded is $T_{\max} = 38.2\,°C$. The thermographic image is produced with Fluke Ti20 Thermal Imager equipment.

6 Conclusions

The linear magnetostrictive motor (LMM) presented in this study is designed as a composite smart structure (CSS). Its core part—the magnetostrictive core (MSC) made of Terfenol-D—is sizable as a morphing CSS.

The LMM is built for optimal performance and packaging; therefore, mathematical modeling and finite element numerical simulations, based on fully coupled magneto-elastic finite element models (FEM) that implement the bidirectional coupling between the magnetic field and structural problems, are used in the design sizing phase. This approach proved also to be realistic, capable of reproducing stationary and dynamic working conditions similar to those for which the LMM is intended.

The numerical simulations conducted for stationary analysis (needed for sizing the LMM) showed off the regions of high magnetic field density (prone to magnetic saturation) and dynamic working (needed to model the real working conditions) are used to validate the design. Numerical simulations conducted for dynamic working conditions predicted the oscillatory motion of the workhead pin of the LMM—basically, the deformation of the MSC—evidenced through experimental measurements.

The LMM with this electronic module drive performs a mechanical oscillation of the active core of Terfenol-D in an extended frequency range, i.e., $f = 1\,\text{Hz} \div 16\,\text{kHz}$. The LMM is composed of the three subassemblies: active central subassembly (A), the coil subassembly (B) and the casing subassembly (C).

The LMM define a family of products because the frequency and duty cycle of PWM voltage applied to the activation coil, respectively the frequency and duty cycle of PWM voltage applied to the bias coil can make establish some specific mechanical characteristics. It is worth mentioning that the frequency of applied voltage to the activation coil is identical with the frequency of applied voltage to the bias coil.
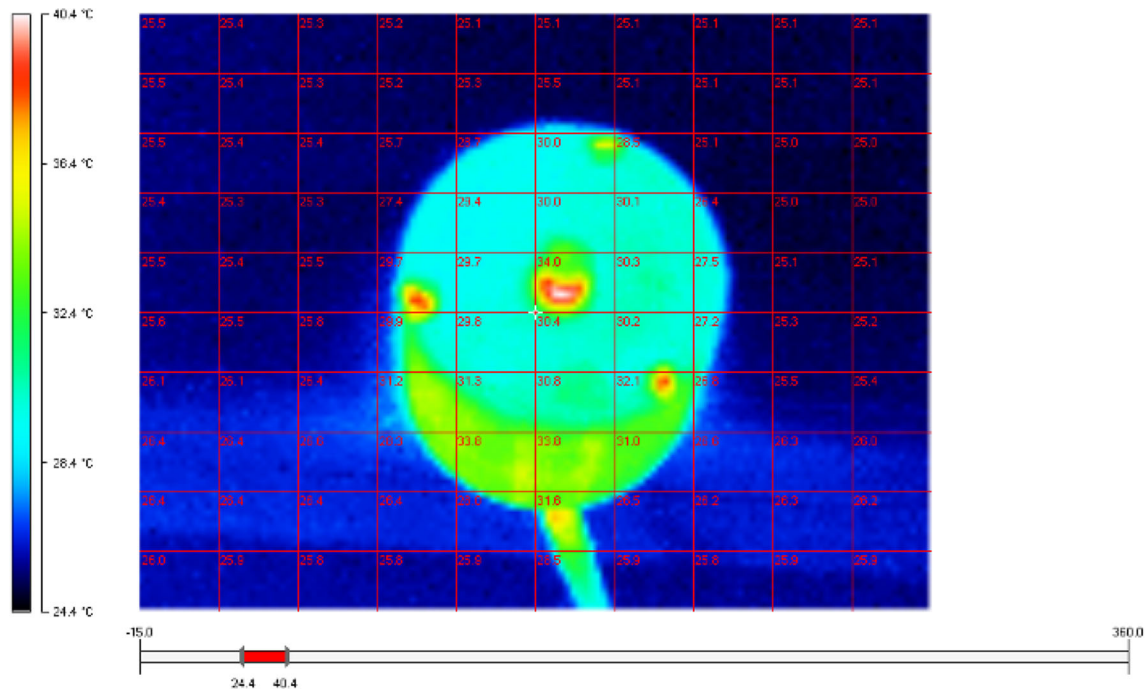
Fig. 19 The temperature field of the LMM after 15 min of operation for $k = 80\%$, at $f = 5$ kHz, as seen from the actuator active end. The passage for the workhead pin is a hot spot region, due maybe to high friction

The construction of the new drive for LMM is centered around the use of the PWM waveform controller DRV101T made by Burr-Brown & Texas Instruments.

If a rectangular shaped TTL signal, with the magnitude $U_d = +5$ V$_{PP}$ and frequency in the range $f = 1$ Hz $\div$ 16 kHz, provided by an external signal generator at the input pin 1 of the PWM DRV101T waveform controller is applied, the Terfenol-D MSC of the LMM is forced into a linear, alternating periodical motion of the same frequency.

On the LMM, several measurements such as interferometry, vibration and thermal imager were performed.

Using an interferometer Agilent 5529B , a diagram of the amplitude function by frequency for the MSC was obtained, using a logarithmic scale with a linear characteristic.

To measure the mechanical vibrations, an accelerometer type PCB353B03, Panasonic, was used. For a fundamental frequency $f = 2500$ Hz, harmonic analysis was performed and it was observed that the amplitude of this harmonics was much smaller than the fundamental.

The thermographic image shows the temperature field of the linear MM, after 1 h of operation. The maximum temperature recorded is $T_{MAX} = 38.2\,°C$.

Authors who are concerned with the control of the combustion processes using different technologies and devices, such as LMMs, conclude that the most appropriate ones are the electronically controlled injectors, which allow for the precise control in real time of the injected mass flow rate. Due to the special properties of the LMMs in terms of operating frequency and force, which were verified experimentally, a lot of practical applications are enabled. Among these, the usage of the LMMs for modulating the fuel admission to the rocket engines is an example.

References

1. ETREMA Products, Inc. (2015) Terfenol-D data sheet. http://www.etrema-usa.com/products/terfenol/. Accessed March 2015
2. Mocanu CI (1980) The electromagnetic field theory. Didactic and Pedagogic Publishing house, Bucharest
3. Chikazumi S (1997) Physics of ferromagnetism. Oxford University Press Inc., New York
4. Engdahl G (ed) (2000) Handbook of giant magnetostrictive materials. Academic press series in electromagnetism, 1st edn. Academic Press, San Diego
5. Moffett MB (1991) Characterization of Terfenol-D for magnetostrictive transducers. JASA 89(3):1448–1455
6. Ignat M, Haraguta CI, Pîslaru-Dănescu L (2007) Aspects about applications of magnetostrictive macroactuator in oil industry. International IEEE Aegean Conference on Electrical Machines and Power Electronics, pp 70–75
7. Lundgren A, Tiberg H, Kvarnsjo L, Bergqvist A, Engdahl G (1993) A magnetostrictive electric generator. IEEE Trans Magn 29:3150–3152

8. Ignat M, Puflea I, Catanescu AL, Vintila A, (2010) Design aspects on the vibration magnetostrictive actuators. XIX International Conference on Electrical Machines (ICEM), pp 1–5

9. Claeyssen F, Lhermet N, Le Letty R (1991) State of the art in the field of magnetostrictive actuators. JASA 89(3):1231–1239

10. You ECS, Hwang W (2004) Design and fabrication of composite smart structures with high electric and mechanical performances for future mobile communication". Mech Compos Mater 40(3):237–246

11. Atulasimha J, Flatau AB (2011) A review of magnetostrictive iron–gallium alloys. Smart Mater Struct 20(4):1–15

12. Morega am, Popa P, Pîslaru-Dănescu L, Morega M (2015) Shape and structure optimization of a magnetostrictive cored actuator, Constructal Law & Second Law Conference, pp 129–138

13. Pîslaru-Dănescu L, Morega AM, Morega M (2011) A novel magnetostrictive injection actuator based on new giant magnetostrictive materials. 7th International Symposium on Advanced Topics in Electrical Engineering, ATEE, pp 331–336

14. Alliance Sensors Group, HG Schaevitz LLC (2015) http://alliancesensors.com/lvit-position-sensors-0. Accessed March 2015

15. AISI (2015) http://www.rgpballs.com/en/products/balls/quick-selection/steel/stainless-steel/hardened-stainless-steel/aisi-420c-stainless-steel-balls. Accessed March 2015

16. Graham F (2009) Development and validation of a bidirectionally coupled magnetoelastic FEM model for current driven magnetostrictive devices. DRUM, University of Maryland, College Park

17. COMSOL Multiphysics, user's guide, 3.5a–4.3a, COMSOL AB, Version 2013, Sweden

18. Burr-Brown & Texas Instruments, PWM Solenoid/Valve Driver, Data Sheet, SBVS008B, January 1998, Revised May 2009, USA

19. Pîslaru–Dănescu L, Panaitescu VN, Ignat M, Stoica V (2007) The use of the electromagnetic actuators in diesel fuel injection systems which are Euro 2 and Euro 3 norm with compliance. Proceeding of 3rd International Conf. on Energy and Environment CIEM

20. Ignat M, Pîslaru-Dănescu L, Puflea I, Zărnescu G, Stoica V, Cătănescu L (2008) Actuatori Electromagnetici. In: Electra ed, Bucharest